Chapter 5

Synthesis, Band gap Engineering and Anomalous photovoltaic Response in $xBaTiO_3$-$(1-x)Bi(Ni_{2/3}Nb_{1/3})O_3$ Solid Solution

5.1 Introduction

The development of lead-free materials for photovoltaic devices is of particular interest because our society demands environment-friendly approaches for energy resources. Multiferroic materials are considered the most promising alternative for ferroelectric photovoltaic devices as they show both ferroelectric and ferromagnetic properties, which provide opportunities to design new optoelectronic devices [T. Choi et al. (2009)]. In Previous chapters, we have reported that Ni and Nb doped $PbTiO_3$ can exhibit semiconducting behaviour at room temperature. Varying the donor or acceptor dopants has been used for lowering the optical band gap of $PbTiO_3$, which can be done by either A-site doping or B-site doping in the perovskite ABO_3 lattice of $PbTiO_3$ [G. Y. Gou et al. (2011)]. Among lead-free multiferroic materials, $BaTiO_3$ has attracted great attention because it shows tunable band gap after transition element doping [S. Das et al. (2018)]. Multiferroic materials based on $BaTiO_3$ (BT) have attracted worldwide attention due to their low toxicity, chemical stability, high dielectric constant and low dielectric loss [M. T. Buscaglia et al. (2006)]. It was previously reported that $BaTiO_3$ single crystal exhibit a bulk photovoltaic effect [R.V. Baltz et al. (1981)].

The main obstacle limiting $BaTiO_3$ as a photo-absorbing layer application in solar cells is its wide band gap which restricts the complete absorption of solar spectrum. The wide band gap of $BaTiO_3$ is due to $3d^0$ configuration of Ti^{4+} ions [V. Mishra et al. (2017)]. Doping of transition-metal ions will substitute Ti^{4+} ion and will decrease the tetragonality and band gap. Research studies have considered doping as an efficient method to lower the band gap and improve the photocurrent response [H. An et al. (2016)]. Several important works highlight the doping of $BaTiO_3$ and role of various dopants to improve the physical properties [G. M. Osara et al. (2016)]. To

reduce the band gap of $BaTiO_3$, various elements such as Mg, Al, Cr, Fe, Co, Zn, Ga, In, Ni etc. are doped in the $BaTiO_3$ at Ti- lattice site [F. Yang et al. (2018); X. K. Wei et al. (2010); D. Phuyal et al. (2018)]. By Mn and Nb co-doping in $BaTiO_3$, reduction in band gap from 3.2eV to 2.7eV is achieved [D. Phuyal et al. (2019)]. Xio et al. have synthesized Bi, Ni doped $BaTiO_3$ with a band gap of 2.06 eV [H. Xiao et al. (2020)]. Though, after this doping, the optical band gap of $BaTiO_3$ is reduced but not low enough to use in solar cells.

Since Nickel is a magnetic ion, Ni doped $BaTiO_3$ system may offer an exciting combination of ferroelectric and magnetic characteristics for multiferroic applications. Introduction of Ni^{2+} at Ti^{4+} site reduces both band gap and ferroelectricity, but Bi^{3+} and Nb^{5+} improve the ferroelectric character [P. Baettig et al. (2005)]. In present work, a new binary system $xBaTiO_3$- $(1-x)Bi(Ni_{2/3}Nb_{1/3})O_3$ has been designed using Bi^{3+}, $Ni^{2+}$and Nb^{5+} ions at Ti^{4+} site. For photovoltaic applications, a suitable ferroelectric semiconductor should have both a large ferroelectric polarization and a low optical band gap. The low band gap of material, help to absorb more photons and its electric field is due to material's remanent polarization that improves the ability to separate the photo-carriers for the current generation.

This chapter presents the results of the study of the optical band gap of $xBaTiO_3$ $-(1-x)Bi(Ni_{2/3}Nb_{1/3})O_3$ (BT-BNN) solid solution in the composition range ($0.50 \leq x \leq 0.92$). Here, Ni^{2+} acts as band gap reducing element while Bi^{3+} and Nb^{5+} will maintain the ferroelectric nature due to its $6s^2$ lone pair electron configuration [P. Baettig et al. (2005)]. The new perovskite ferroelectric solid solution xBT-(1-x)BNN has been synthesized by solid state reaction method and its physical properties were investigated with varying the $Bi(Ni_{2/3}Nb_{1/3})O_3$ (BNN) doping concentration. In this study, we mainly demonstrate the effect of BNN doping on structural, morphological,

ferroelectric, semi-conducting properties and optical band gap of xBT-(1-x)BNN ceramic. To confirm the photovoltaic nature of xBT-(1-x)BNN, photovoltaic cells with device structure AZO/BT-BNN/Ag were fabricated, and their photo-electrical properties were measured. The observed bulk photovoltaic behaviour and its mechanism in BT-BNN polycrystalline multiferroic materials is also discussed.

5.2 Experimental

Various compositions of $xBaTiO_3$-(1-x)$Bi(Ni_{2/3}Nb_{1/3})O_3$ (BT-BNN) with $0.50 \leq x \leq 0.92$ were synthesized by conventional solid state route of 'ceramic preparation'. The detail of synthesis route is presented in chapter-2. Stoichiometric weights of constituent reactants, i.e., $BaCO_3$, TiO_2, Bi_2O_3, TiO_2, Nb_2O_5 and NiO were first mixed with the help of a mortar-pestle. The mixed powders were ball-milled in acetone medium with zirconia balls. The ball milled powders were calcined in the temperature range of 600 ^oC to 950 ^oC inside furnace. Powder X-ray diffraction (XRD) measurements were performed at room temperature from 20^o to 120^o using RIGAKU MINIFLEX 600, powder x- ray diffractometer with Cu-K_α radiations. Crystal structure analysis was done by Rietveld refinement using FULLPROF suite [J.R. Carvajal (1993)]. The microstructures of as prepared BT-BNN ceramics were examined using a scanning electron microscope (ZEISS, Evo 18 Research). The ferroelectric polarization as a function of external field was examined by Radiant ferroelectric tester based on standard Sawyer-Tower circuit, in frequency range from 1 to 1000 Hz, at room temperature. The UltraViolet-visible (UV-Vis) absorbance spectra recorded at room temperature using Horiba Jobin Yvon, Spectrophotometer, and the optical band gaps were calculated by Tauc equation plots. In order to study ferroelectric photovoltaic phenomenon in BT-BNN, thin pellets of BT-BNN are prepared and mounted on silicon wafer using silver epoxy. The ZnO:Al (AZO) thin film was deposited on top of pellet

which acts as transparent electrode. The current –voltage (I-V) measurement of as prepared device were measured using Keithley-2400 source- meter, interfaced with a computer. A green laser light (wavelength ~ 532 nm, 5-50mW power) and visible light were used to illuminate the device surface.

5.3 Results and Discussion

5.3.1 Composition Dependent Structural analysis of $xBaTiO_3$-(1-x)$Bi(Ni_{2/3}Nb_{1/3})O_3$ Solid Solution in the Composition Range ($0.60 \leq x \leq 0.92$).

Room-temperature powder XRD patterns for $xBaTiO_3$-(1-x)$Bi(Ni_{2/3}Nb_{1/3})O_3$ (BT-BNN) solid solution for the compositions with x = 0.92, 0.85, 0.80, 0.75, 0.70 and 0.60, in the 2θ range of 20^o to 120^o, are shown in Fig. 5.1. These XRD patterns of synthesized BT-BNN compositions are consistent with that expected for ideal cubic ABO_3 perovskite structure. No additional XRD peaks of any impurity phase are seen in Fig. 5.1. The XRD profiles for all the compositions of BT-BNN do not show any clear splitting and appear to be a singlet. In view of this, we refined the structure of all the compositions using cubic symmetry with space group *Pm*3*m*. Rietveld structure refinements were carried out using FULLPROF suite [Carvajal (2011)]. The Rietveld method is used for the precise structural analysis and quantitative phase analysis of crystalline materials. Rietveld method fits an approximated structural model to the experimental data to get the precise structural parameters.

In the Rietveld refinement process, least square method is used to fit the XRD patterns. In the least square method, theoretical XRD profile is generated using the starting structural model. The theoretically obtained XRD profile is tried to match with the experimental XRD profile by adjusting the instrumental and structural parameters. During the refinement process, the difference between theoretical and experimental patterns is minimised to an acceptable level by refining instrumental and structural

parameters. In the refinement process of experimental data, various agreement factors are used to quantitatively ascertain the quality of fit between experimental and calculated patterns. In Rietveld method, various profile functions have been suggested to define the peak shape of the calculated XRD pattern. Pseudo-Voigt is widely used, which is the linear combination of Lorentzian and Gaussian function.

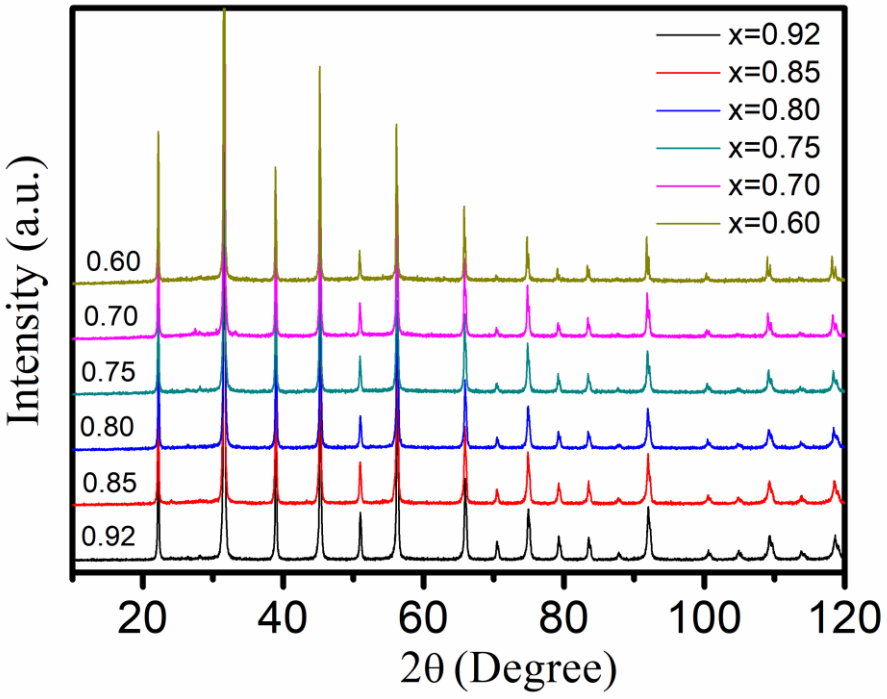

Figure 5.1 Powder x-ray diffraction patterns of $xBaTiO_3$-(1-x)$Bi(Ni_{2/3}Nb_{1/3})O_3$ solid solution in the composition range ($0.60 \leq x \leq 0.92$).

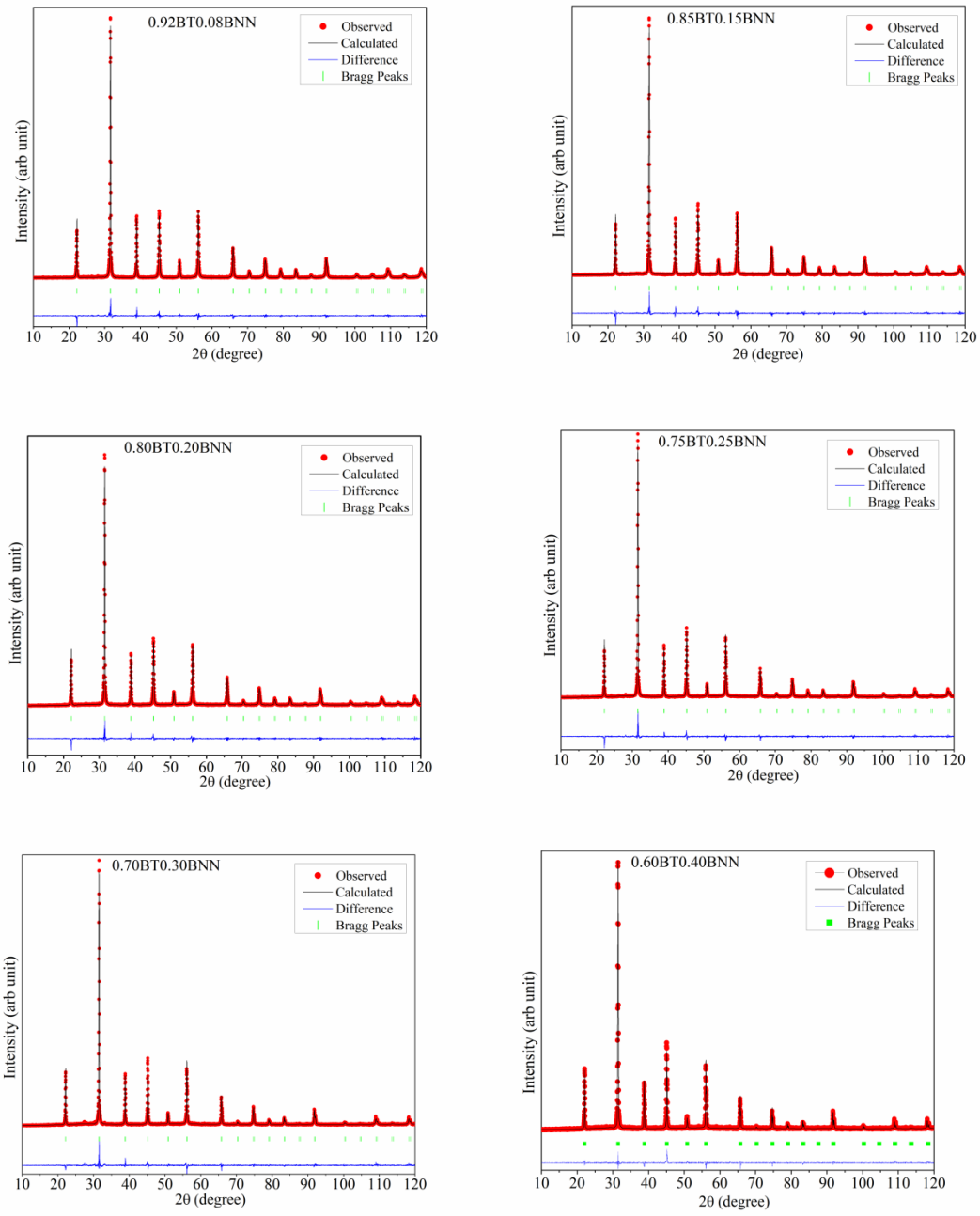

Figure 5.2 Rietveld fit for the XRD patterns of $xBaTiO_3$-(1-x)$Bi(Ni_{2/3}Nb_{1/3})O_3$ ceramics with x=0.92, 0.85, 0.80, 0.75, 0.70 and 0.60. Dots indicate experimental XRD data, overlapping calculated XRD pattern is shown by continuous line. The lower curve shows the difference between experimental and calculated XRD patterns. Vertical bars indicate position of Bragg's peaks.

The initial refinements were carried out by varying zero-point shift, the unit cell parameters and background parameters. In the refinement process, the background was modelled using 5^{th} order polynomial and peak shapes were modelled by Pseudo-Voigt function. Occupancy parameters of all the ions were fixed at the nominal composition during refinement. At advanced stage, various parameters like background, lattice parameters, zero-correction, thermal parameters, half width parameters (U, V and W) were varied during refinement. The Wyckoff positions and the asymmetric unit for cubic space group were used during Rietveld refinement of structures of BT-BNN system. In the process of Rietveld refinement, we considered the substitution of Bi^{3+} ions on Ba-site, while Ni^{2+} ions and Nb^{5+} on Ti-site. In the cubic phase with *Pm*3*m* space group, the Ba^{2+}/Bi^{3+} ions occupy 1(a) sites at (0, 0, 0), $Ti^{4+}/Ni^{2+}/Nb^{5+}$ ions occupy 1(b) sites at (1/2, 1/2, 1/2) and $O^{2-}(1)$ occupy 3(c) sites at (1/2, 1/2, 0), and $O^{2-}(2)$ occupy 3(d) sites at (1/2, 0, 1/2).

Fig. 5.2 shows the Rietveld fit for the XRD profile of different compositions of BT-BNN. The dots in Fig. 5.2 indicate the experimental XRD data and overlapping continuous curve shows the calculated XRD pattern. The lowest curve shows the difference between observed and calculated XRD profiles. The vertical bars between fitted and difference profiles indicate the positions of Bragg's reflections. A very good fit between observed and calculated XRD patterns confirms the cubic structure with *Pm*3*m* space group for all the compositions. It is clear from Fig.5.2, that (200) profile is singlet and no asymmetry or splitting is observed in lower 2θ side for any tetragonal splitting. Thus, the structure of BT-BNN composition is cubic in nature with space group *Pm*3*m*. The Rietveld structural analysis of the other compositions also confirms the cubic structure with space group *Pm*3*m* as shown in Fig.5.2.

All the compositions of BT-BNN solid solutions are refined to get the structural parameters. Lattice parameters, unit cell volume and bond lengths have been obtained from the Rietveld refinement. All these calculated parameters obtained from Rietveld structure refinement are presented in Table 5.1. The lattice parameter (a) has increasing trend with increasing the BNN content. The lattice parameter for 0.92BT-0.08BNN composition is 4.00754 (1)Å which increases to 4.01675 (1)Å for 0.60BT-0.40BNN. With increase in BNN dopant concentration, the unit cell volume increases which can be attributed to the substitution of larger Ni^{2+} cations (0.69Å) for smaller Ti^{4+} cations (0.605Å). The larger ionic radius of Ni^{2+} also causes a small structural lattice expansion, thus Ni^{2+} doping can promotes the lattice distortion. Fig.5.3 depicts the variation in bond length (Bi-O and Ni-O) with composition for BT-BNN solid solution. It has been observed that for x= 0.92, corresponding Bi-O bond length is 2.8338(1) Å. Whereas for x=0.60, corresponding Bi-O bond length is 2.8403 Å. It shows that with inclusion of Ni^{2+} cations (0.69Å) for smaller Ti^{4+} cations (0.605Å), the Bi-O bond length increases with increasing the BNN doping concentration in BT. The Ni-O bond length is slightly increased.

Table 5.1: Refined structural parameters and bond lengths for xBT-(1-x)BNN solid solutions obtained by using Rietveld refined structural parameters.

x	Lattice Parameters a=b=c (Å)	Unit Cell Volume ($Å^3$)	Density (gm/cc)	Bond length Bi-O (Å)	Bond length Ni-O (Å)
0.92	4.00754(1)	64.3627	6.202	2.8338(1)	2.0038(1)
0.85	4.00872(2)	64.4195	6.374	2.8396(1)	2.0044(1)
0.80	4.01083(1)	64.5214	6.485	2.8361(1)	2.0054(1)
0.75	4.01195(3)	64.5751	6.601	2.8369(1)	2.0060(1)
0.70	4.01387(2)	64.6681	6.712	2.8382(1)	2.0070(1)
0.60	4.01675(1)	64.8071	6.938	2.8403(1)	2.0084(1)

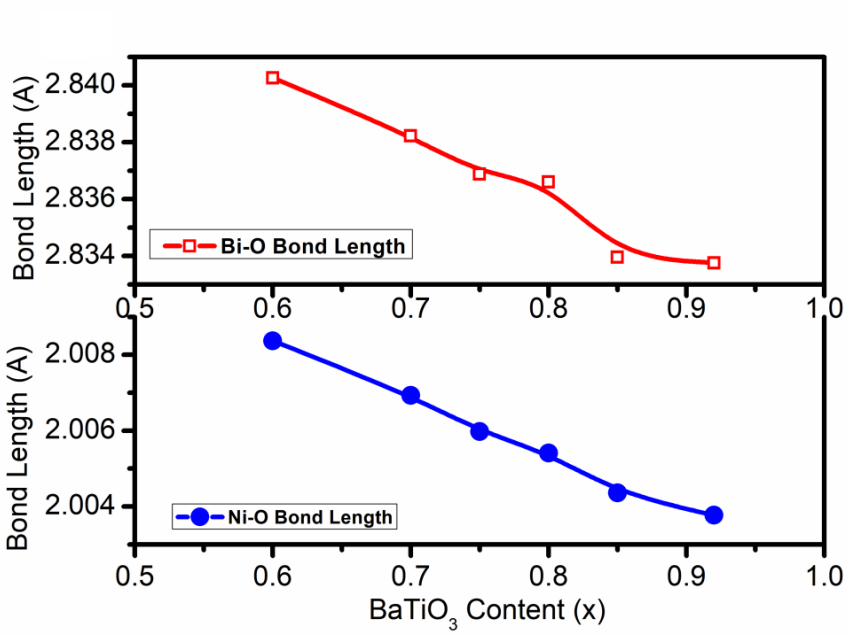

Figure 5.3 Variations of Bond length (a) Bi/Ba-O and (b) Ni/Nb/Ti-O for cubic phase of various compositions of $xBaTiO_3$-(1-x)$Bi(Ni_{2/3}Nb_{1/3})O_3$ obtained after Rietveld refinement.

5.3.2 Microstructure of $xBaTiO_3$-(1-x)$Bi(Ni_{2/3}Nb_{1/3})O_3$ Solid Solution in the Composition Range ($0.50 \leq x \leq 0.92$).

Fig. 5.4 depicts the SEM images of xBT-(1-x)BNN compositions with x = 0.92 0.80 and 0.60. It is observed that microstructure and grain size of BT-BNN ceramics is affected by the BNN concentration in the solid solution. With increasing the BNN content, the grain size increases as can be observed from Fig. 5.4 (a), (c) and (e). For 0.92BT-BNN, grain size is in the range 400 nm to 1 µm while for 0.80BT-BNN grain size increases in the range of 570 nm – 3.1 µm. For 0.60BT-BNN, the grain size is in the range from 1.0 µm to 6.5 µm. The SEM images reveal that with increasing the BNN content, the grain size increases and non-uniformity in grain size also increases. The increase in grain size can be related to Ni^{2+} and Nb^{5+} doping which is previously reported [D. Kolar et al (1998)]. Presence of Bi also promotes the densification as Bi-

based oxides have lower melting point. Any local melting of Bi-based oxide during sintering can promote high densification and grain growth by liquid phase sintering.

The energy dispersive X-ray spectra (EDS) map for xBT-(1-x)BNN compositions with x = 0.92, 0.80 and 0.60 is shown in Fig. 5.4 (b), (d) and (e). In EDS, presence of the characteristic peaks of constituent elements confirms the elemental composition of the synthesized solid solution. EDS analysis confirms the presence of Ba, Ti, Ni, Nb, Bi, and O elements. No other impurity element is found in the samples. Fig. 5.5 shows the elemental mapping of $xBaTiO_3$-(1-x)$Bi(Ni_{2/3}Nb_{1/3})O_3$ for the compositions with x=0.92 and 0.60. From the elemental map, it is clearly seen that with increasing the BNN doping concentration the distribution of Ni, Nb. And Bi increases while percentage distribution of Ba and Ti reduces.

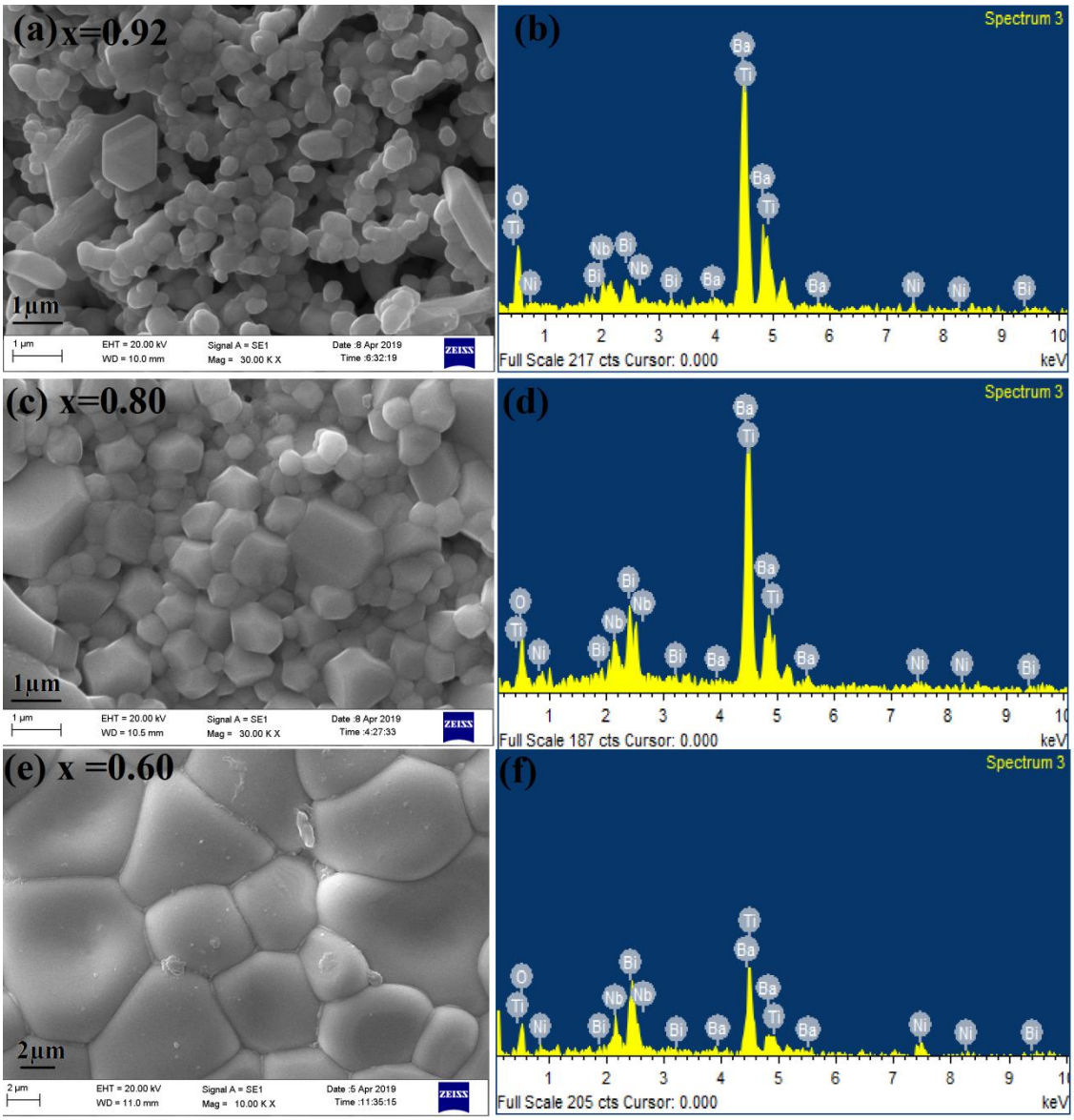

Figure 5.4 The Scanning electron microscopy (SEM) images of (a) 0.92BT-0.08BNN, (c) 0.80BT-0.20BNN and (e) 0.60BT-0.40BNN ceramics, (b), (d) and (f) showing the Corresponding Energy dispersive X-ray spectroscopy (EDS) spectrum.

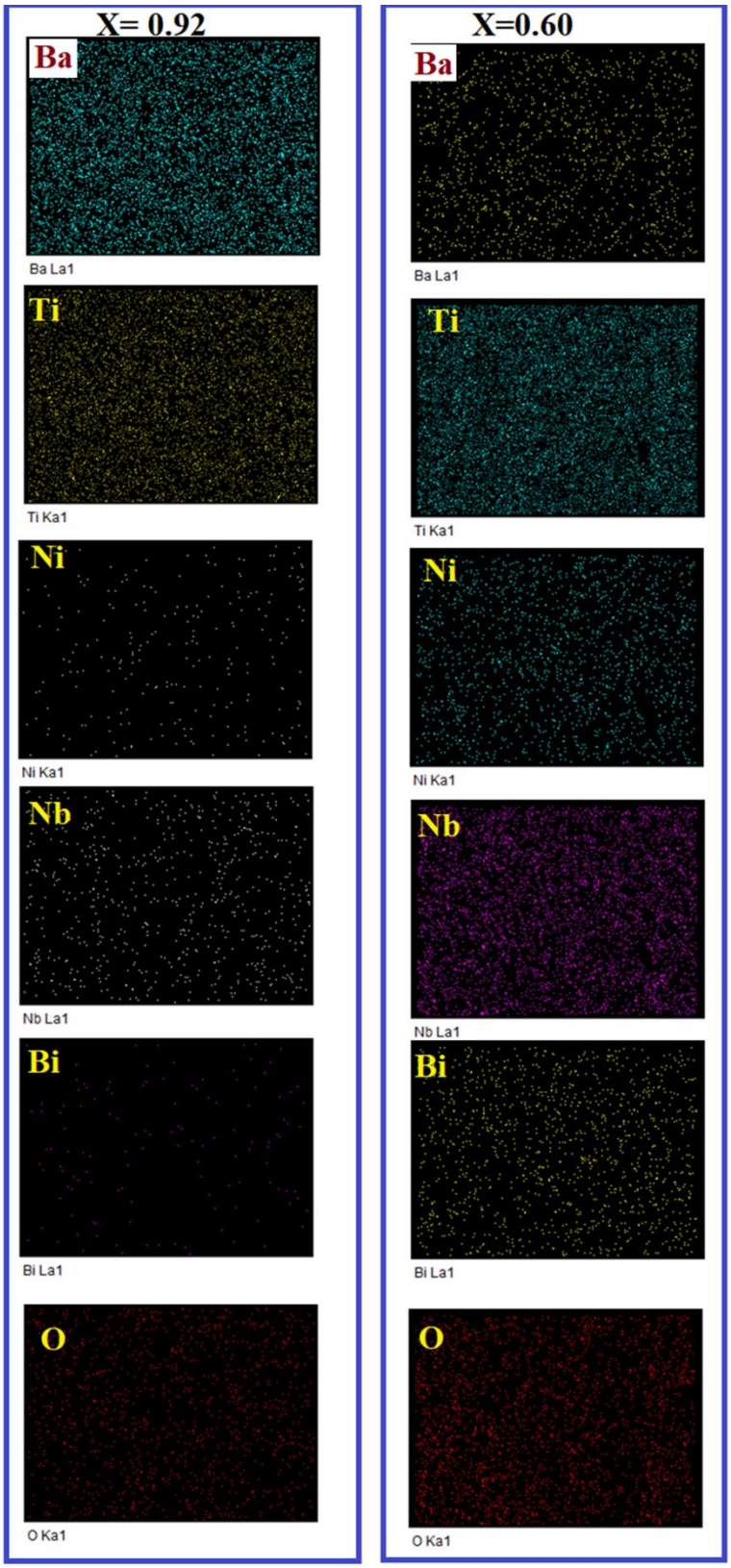

Figure 5.5 The EDS elemental map of $xBaTiO_3$-(1-x)$Bi(Ni_{2/3}Nb_{1/3})O_3$ ceramics with compositions x=0.92 (left panel) and x=0.60 (right panel).

5.3.3 Composition Dependent Ferroelectric and Electrical Behaviour of $xBaTiO_3$-$(1-x)Bi(Ni_{2/3}Nb_{1/3})O_3$ Solid Solution ($0.50 \leq x \leq 0.92$).

The existence of ferroelectric polarization is crucial and non-ignorable in perovskite materials for their application in ferro-photovoltaic devices. For realization of ferroelectric photovoltaic effect in materials, they should possess the polarization at room temperature. The ferroelectric polarization hysteresis loops for various compositions of BT-BNN were measured at room temperature and are shown in Fig. 5.6. It is observed that even though BT-BNN has cubic structure, still it shows the ferroelectric nature with well-defined hysteresis loop and non-zero remanent polarization. Presence of vacancies and local structural distortion in the structure due to Bi and Nb doping may be attributed to the ferroelectricity in these compositions. As shown in Fig. 5.6 (a), (b), (c) and (d), all the investigated compositions of BT-BNN exhibit ferroelectricity. Fig. 5.6 (a) shows the P-E hysteresis loops of the 0.92BT-0.08BNN composition measured at frequency f= 1Hz at various electric field (f = 15, 20, 23, 25, 27 kV/cm) which indicates that 0.92BT-0.08BNN ceramics has good ferroelectric response. In 0.92BT-0.08BNN composition, P_s of 6.52 $\mu C/cm^2$, P_r of 1.11 $\mu C/cm^2$ and E_c of 4.0 kV/cm are observed under the maximum applied electric field of 27 kV/cm and 1Hz frequency. Fig. 5.6 (b) depicts the P-E loops of 0.75BT-0.25BNN composition measured at f = 2Hz with varying the electric field (E = 10, 20 and 30 kV/cm). It can be seen that the shape of the P-E hysteresis loop does not depend on applied electric field. In 0.75BT-0.25BNN composition, P_s of 4.55 $\mu C/cm^{2,}$, Pr of 2.02 $\mu C/cm^2$ and E_c of 9.3 kV/cm are observed for the electric field of 30 kV/cm and frequency 2 Hz. Fig. 5.6 (c) depicts the P-E loops of 0.60BT-0.40BNN composition measured at f = 10Hz with varying electric field (E = 20, 30 and 40 kV/cm). Fig. 5.6 (d) depicts the P-E loops of 0.50BT-0.50BNN composition measured at f = 1Hz with

varying electric field (E = 20, 30 and 35 kV/cm). In 0.50BT-0.50BNN composition, P_s of 2.14 μC/cm^2, P_r of 1.05 μC/cm^2 and E_c of 11.7 kV/cm are observed for the electric field of 35 kV/cm and frequency 1 Hz. The remnant polarization (P_r) increases with increasing the applied electric field. The low P_r value is due to large leakage currents of the dielectric which makes the BT-BNN ceramic difficult to be fully polarized, as the coercive field (E_c) is varying with the applied electric field.

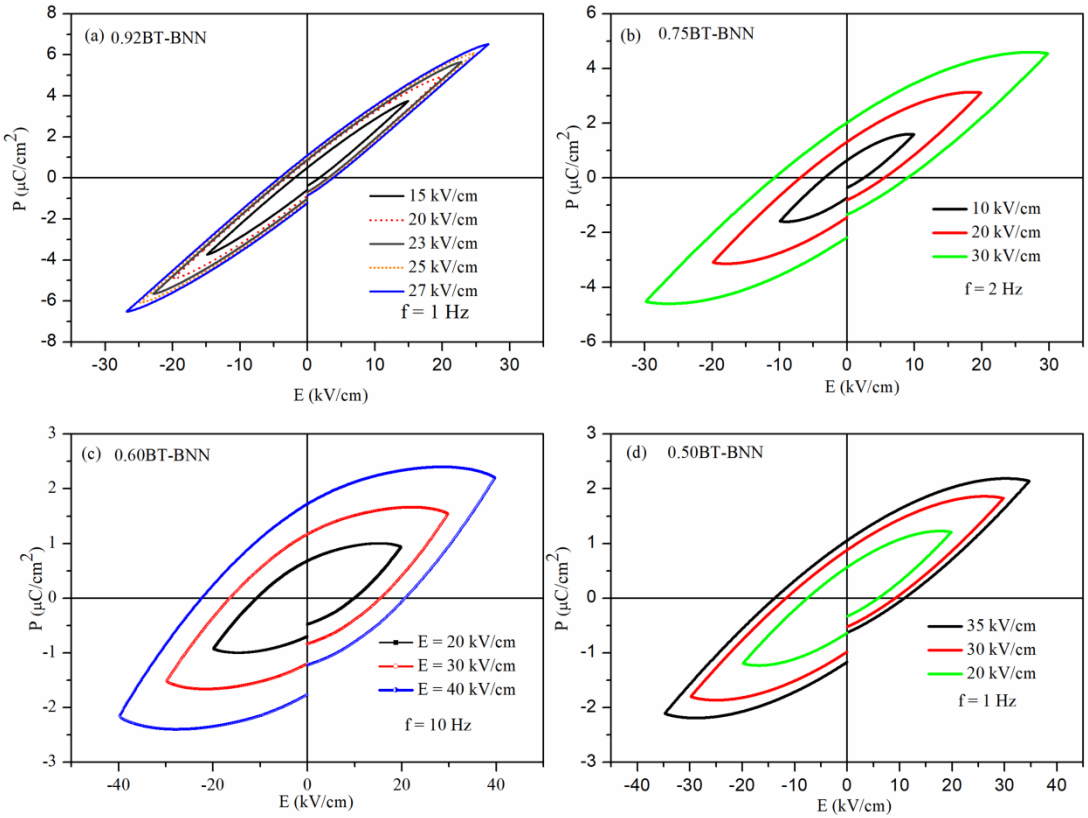

Figure 5.6 Room temperature P-E hysteresis loops for the $xBaTiO_3$-(1-x)$Bi(Ni_{2/3}Nb_{1/3})O_3$ ceramics with the compositions (a) x=0.92 (b) x=0.75 (c) x=0.60 and (d) x=0.50 recorded at different applied electric field.

The room temperature measured Nyquist plot (Z′ vs Z″) of 0.92BT-0.08BNN, 0.80BT-0.20BNN, 0.60BT-0.40BNN and 0.50BT-0.50BNN compositions is shown in Fig. 5.7. The Nyquist plot consist two semi-circular arcs which corresponds to the electrical contribution of bulk (grain interior) and grain boundaries (intergranular

activities). As shown in Fig. 5.7 (a), impedance analysis was done from room temperature to 600°C and Nyquist plot at selected temperatures is compared for 0.92BT-0.08BNN. From intercept of semi-circular arcs on the real Z′ axis the R_g and R_{gb} values are estimated from the Nyquist plot. Both R_g and R_{gb} values decrease with increasing the temperature, which confirm the negative temperature coefficient of resistivity (NTCR). The NTCR process is caused by thermally activated charge carriers in semiconducting materials. Thus, it confirms that BT-BNN ceramic can be considered as ferroelectric semiconductor [Q. Xu et al. (2016)]. In present work, Ag electrode is used on both sides of pellets for electrical characterization. No electrode interface response is detected at low frequencies in Nyquist plots, which indicate that only electronic charge carriers are dominant [Y. Huang et al. (2013)].

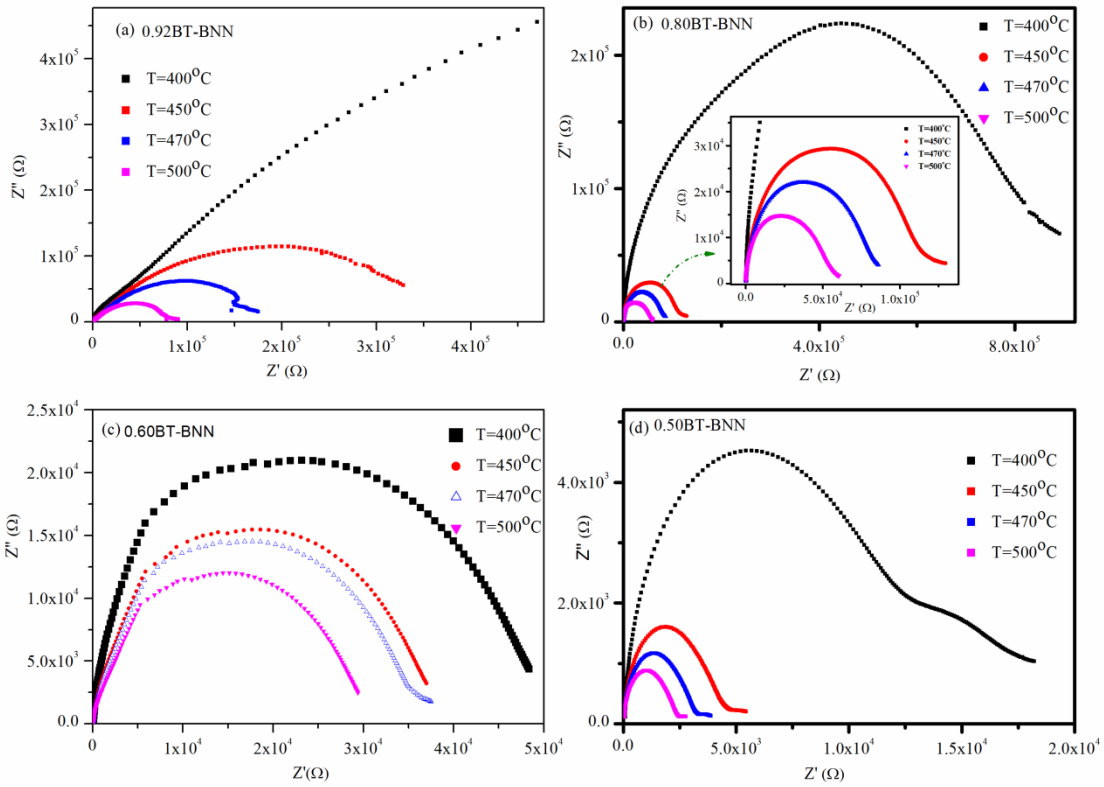

Figure 5.7 Nyquist plots (Z' vs Z'') for (a) 0.92BT-0.08BNN (b) 0.80BT-0.20BNN (c) 0.60T-0.40BNN and (d) 0.50BT-0.50BNN compositions measured at different temperatures.

5.3.4 Composition Dependent Optical Band gap Analysis of $xBaTiO_3$-(1-x)$Bi(Ni_{2/3}Nb_{1/3})O_3$ Solid Solution in the Composition Range ($0.50 \leq x \leq 0.92$).

We characterized the light-absorption properties of the BT-BNN samples using UV-visible spectroscopy. The UV-visible absorption spectrum reveals the information regarding the possibility of material's application as photoactive layer in photovoltaic devices. In order to calculate band gap of BT-BNN, UV-visible absorption spectra of all samples were measured. Fig. 5.8(a) shows the absorption spectra of various compositions of BT-BNN. It is observed that absorption spectra have multi-absorption peaks (mentioned in Fig as A1 and A2). The A2 absorbance peak, in range 680-820 nm, is more prominent for higher doping percentage of BNN in BT-BNN. The absorbance peak in NIR region can be attributed to the presence of oxygen vacancies. These oxygen vacancies are due to presence of BNN doping in BT-BNN solid solutions as this peak is absent in pure BT absorption spectra. The broad absorption band edge in the range 400-500 nm is resulting due to overlap of field transfer transitions and transition from ligand field. Absorption below 450 nm wavelength is associated with d-d transition (charge transfer transition) [B. Ramachandran et al. (2010)]. The shift of absorption edge toward larger wavelength is indication of lowering of optical band gap.

The Indirect optical band gap of BT-BNN in the composition range ($0.20 \leq x \leq 0.50$) is calculated using Tauc plot, $(\alpha h\upsilon)^{0.5}$ vs $h\upsilon$, where $h\upsilon$ is band gap energy and α is the absorption coefficient. As shown in Fig 5.8 (b), the observed indirect band gap of BT-BNN reduces from 1.75 eV to 1.3eV, with increasing the BNN content from x = 0.20 to x = 0.50. The direct band gaps of all the compositions were determined by extrapolating the linear part of the $(\alpha h\upsilon)^2$ versus $(h\upsilon)$ plots, where $h\upsilon$ is the direct band gap energy and α is absorption coefficient [J. Tauc et al. (1966)]. As shown in Fig.

5.8(c), the Tauc equation plots, $(\alpha h\upsilon)^2$ vs $h\upsilon$, for direct band gap provide reasonable band gap values.

The undoped $BaTiO_3$ shows an optical band gap 3.2 eV, as depicted in Fig. 5.8(f). The band gap of $BaTiO_3$ reduces to 2.48 eV with 20% BNN (x = 0.80) doping as shown in Fig. 5.8(c). Two different band gaps E_{g1} = 2.48 eV and E_{g2} = 1.22 eV were featured in $(\alpha h\upsilon)^2$ vs $h\upsilon$ plot for 0.80BT-0.20BNN solid solution. The main band gap (E_{g1}) value reduces to E_{g1} = 2.19 eV, while secondary band gap (E_{g2}) = 1.32 eV is slightly increased for 0.60BT-0.40BNN. This change in band gap with increasing the BNN doping concentration can be explained in terms of change in crystallite size, density, unit cell volume and bond length. As listed in table 5.1 and shown in Fig. 5.3, the bond length Bi-O slightly increases with increasing the BNN content, and bond length of cubic phase is much smaller than the tetragonal phase of pure BT. Mishra et al. have reported that theoretically calculated band gap of cubic BT is lower than the tetragonal phase because in conduction band, the contribution of d_{xy} and d_{yz} reduces in material for cubic phase [V. Mishra et al. (2018)]. A gap state is also introduced by an acceptor $Ni^{2+}3d_z^2$ energy level.

The observed lowering of optical band gap of BT-BNN may be related to increased oxygen vacancies with higher BNN doping. The oxygen vacancies create new sub-bands of defect induced energy states. The sub-bands reduce the gap between conduction and impurity band which reduces the optical band gap of BT-BNN solid solution. With further increase in BNN doping to 50%, an unusual increase in band gap is observed which can be related to the impurity formation near grain boundaries.

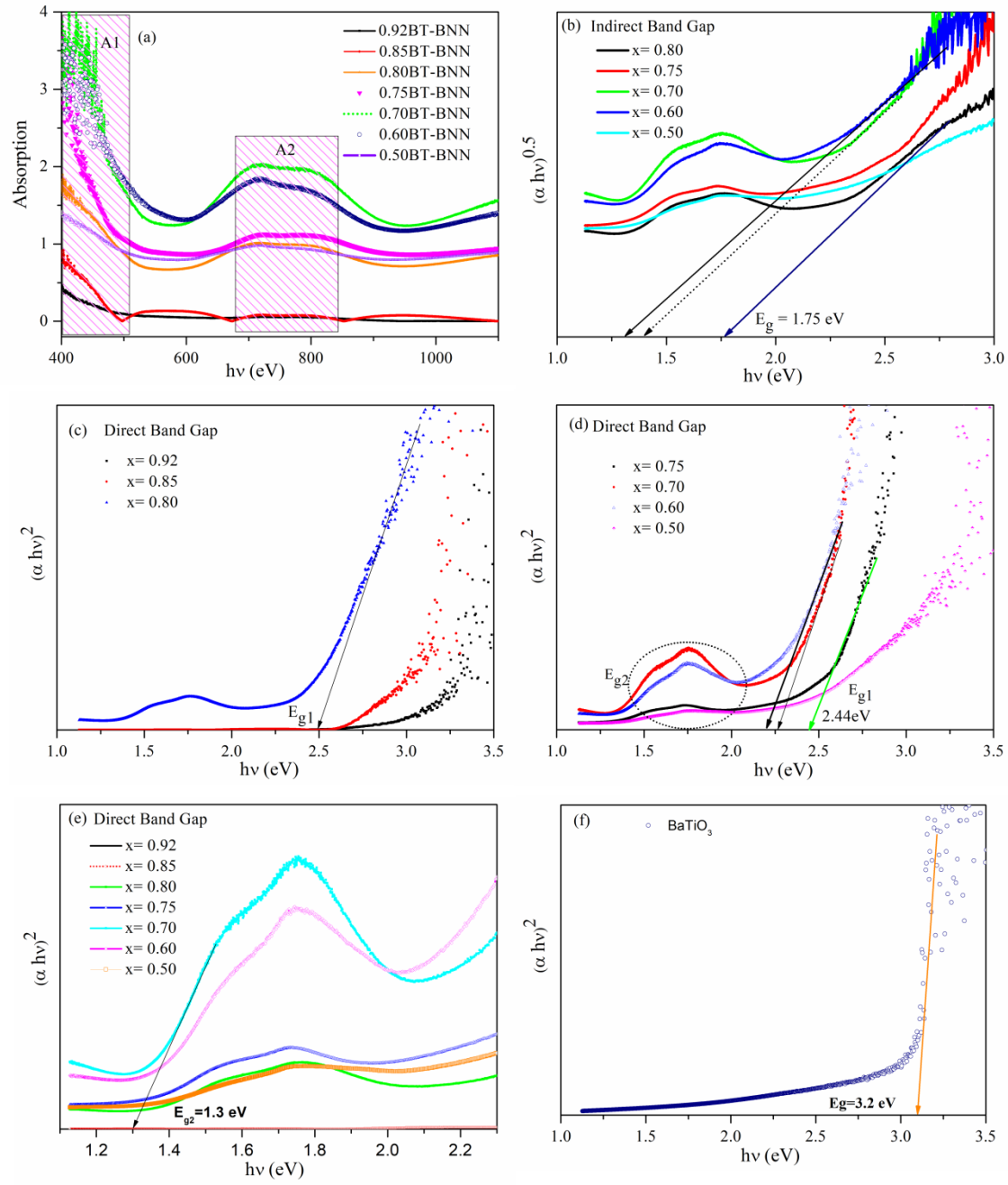

Figure 5.8 Composition dependent variations of (a) absorption spectra; (b) Estimated indirect band gap using the Tauc plot $(\alpha h\upsilon)^{0.5}$ vs hυ; (c) and (d) Estimated direct band gap using the Tauc plot $(\alpha h\upsilon)^2$ vs hυ, for $xPbTiO_3$-(1-x)$Bi(Ni_{1/2}Ti_{1/2})O_3$ solid solution in the composition range ($0.50 \leq x \leq 0.92$); (e) Direct band gap E_{g2} and (f) the Tauc plot $(\alpha h\upsilon)^2$ vs hυ for undoped $BaTiO_3$. The tangent line for linear region is used to estimate the band gap.

To further investigate the effect of Ni and Nb doping in band gap of BT, new compositions $BaTi_{(1-x)}Ni_xO_3$ and $BaTi_{(1-x)}(Ni_{1/3}Nb_{2/3})_xO_3$ were prepared. It is observed that band gap E_{g1} reduces from 3.2eV to 2.56eV when BT is doped with 7% NiO and it further reduces to 2.05eV for 9% NiO doping. When Ni and Nb both are co-doped at Ti-site in $BaTiO_3$, the lowest band gap 2.06 is obtained for 7% ($Ni_{1/3}Nb_{2/3}$) doping. These results indicate that Nb doping is not affecting much the optical band gap of $BaTiO_3$ and second band gap (E_{g2}) is absent, as shown in Fig.5.9. So, in BT-BNN solid solutions, presence of E_{g2} band gap at low energy side makes it more useful for photo-absorbing layer.

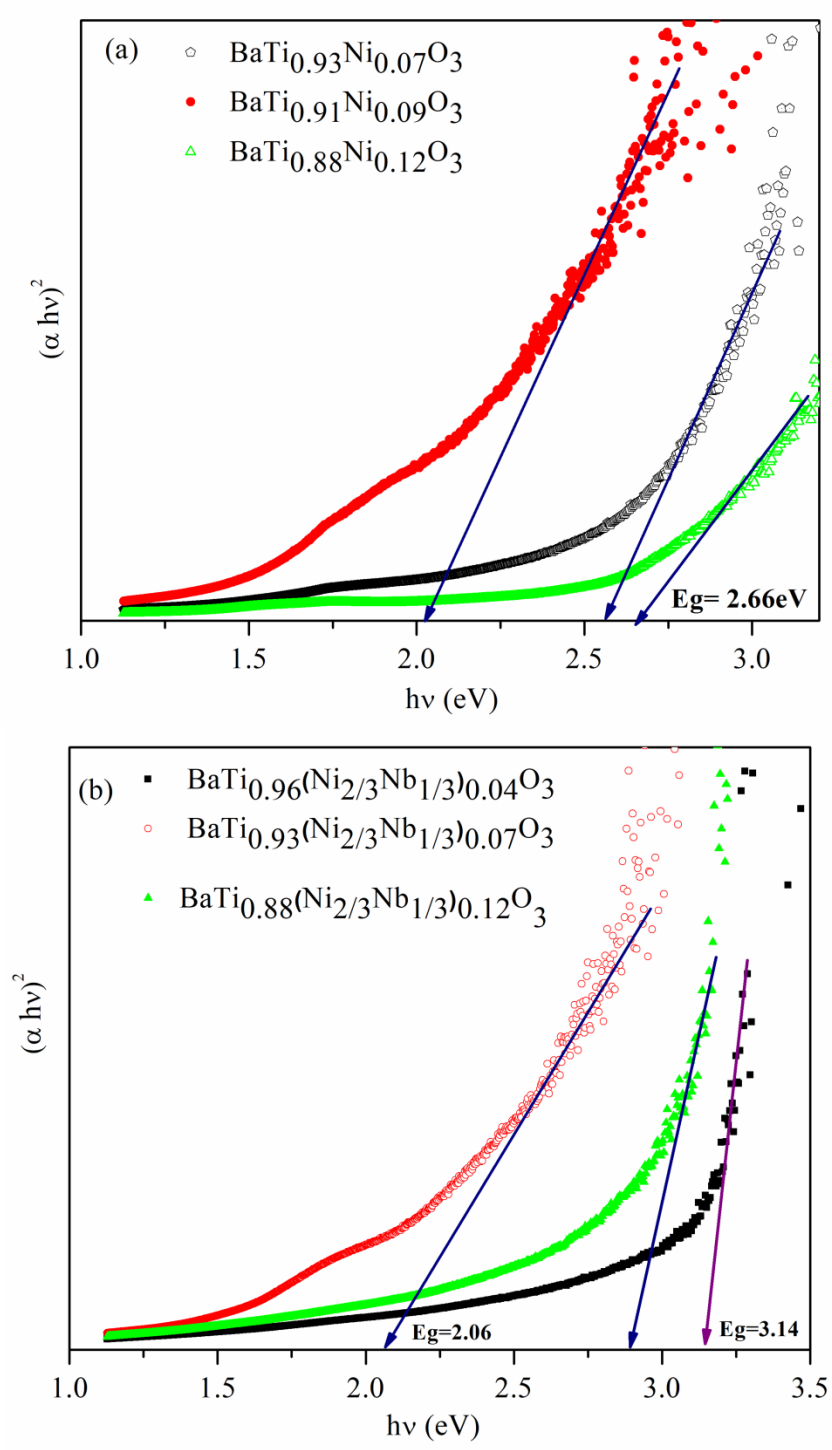

Figure 5.9 Direct band gap for (a) Varying Ni doping in $BaTi_{(1-x)}Ni_xO_3$ solid solution (b) Varying Ni and Nb co-doping in $BaTi_{(1-x)}(Ni_{1/3}Nb_{2/3})_xO_3$ solid solution.

The mechanism of band gap lowering due to formation of sub-bands between valence and conduction band is explained schematically in Fig.5.10. Theoretically, it is known that the B-site substitution of ABO_3 with an oxygen vacancy stabilized d^8M^{2+} cation (d^8Ni^{2+}) could decrease the band gap while maintaining the polarization in the solid solution. In $BaTiO_3$, the valence band (V.B.) is created by O-2p orbitals which interact with 3d state of Ti ion. The conduction band (C.B.) is formed from Ti 3d states. When Ni^{2+} is doped, it replaces Ti. Both C.B. and V.B. get localized around Ni-3d states. The Ni-d_z^2 state is above V.B. and Ni-d^2_{x-y} will be below C.B. state [G.Y. Gou et al. (2011)]. The Ni-3d state will be below main Ti-3d state as its energy is lower than Ti-3d. So, Ni-3d state will increase the tailing of conduction band edge, as shown in Fig 5.10 (c) [W. Zhou et al. (2015)]. The reduced band gap in BT-BNN is due to inter-band transition from the d_z^2 state to the $d_{x^2-y^2}$ state [F. Azough et al. (2010)].

The solid solution BT-BNN with more than 20% BNN doping shows two direct band gaps. The E_{g1} band gap feature is stronger and visible in Tauc plot as around this region the absorption is high. As shown in Fig.5.10 (d-e), the direct band gap E_{g1} arises from p-d charge-transfer excitations. The band gap at lower energy side E_{g2}, arises from hybridization of Ni ($3d_z^2$+$O2p_z$) and Ni-3d excitations [B. S. Holinsworth et al. (2015)]. The E_{g2} feature is weaker in intensity, which may be due to lower density of states. The position of E_{g1} and E_{g2} band gap is explained by showing the sub-band states. The obtained narrower band gap of BT-BNN solid solutions reveals that 0.70BT-0.30BNN have ability to absorb the highest amount of incident photons and smooth transition of electrons from valence band (V.B.) to conduction band (C.B.) can enhance the photo-current in BT-BNN based solar cells.

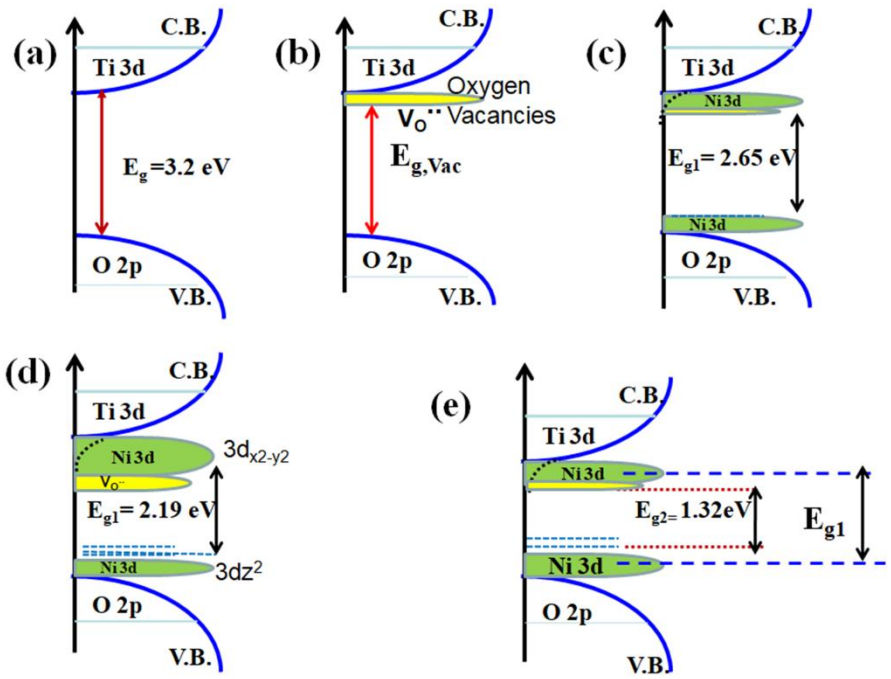

Figure 5.10 Schematic diagram of density of electronic states (a) Ideal Situation for $BaTiO_3$ (b) With presence of oxygen vacancies (c) with presence of Ni^{2+} 3d states (d) For higher doping percentage of BNN and (e) E_{g1} and E_{g2} band gap in xBT-(1-x)BNN.

5.3.5 Light Intensity Dependent Current Density (J) - voltage (V) Characteristics of AZO/BT-BNN/Ag Device

The photoelectrical measurements on BT-BNN based heterostructures were performed to study its photovoltaic behaviour. The composition 0.70BT-0.30BNN was selected to investigate, the effect of light illumination intensity on photovoltaic response of as prepared solid solution because this composition has low band gap region and minimum required polarization. The ferroelectric ceramics were polished to a thickness of ~ 600 µm and mounted on a silicon wafer with silver paste. This silver paste served as the bottom electrode after drying at 500°C. For top electrode, thin film of ZnO:Al (AZO) was deposited on BT-BNN surface by magnetron sputtering. The circular top electrode was fabricated on BT-BNN surface using patterned shadow mask and at

200°C substrate temperature for better adhesion of film. The thickness of AZO layer was determined to be ~ 150 nm with resistance of less than 200Ω.

A Schematic illustration of various fabrication process steps of AZO/BT-BNN/Ag heterojunction device is shown in Fig. 5.11. The thin BT-BNN pellet was sandwiched between two electrodes. Fig 5.12 depicts the representative device configuration during I-V measurement with AZO/BT-BNN/Ag, where Ag acts as bottom electrode and AZO acts as top electrode. The pellets were poled before I-V measurements at 100°C for 30 minutes. The poling voltage was decided according to thickness of pellets and coercive field of BT-BNN composition. The negative applied voltage from top electrode (AZO) to the bottom electrode (Ag) is termed as a negative polarization state and positive voltage applied from the top electrode to the bottom electrode is defined as positive polarization state. In other term, the upward polarization state and downward polarization states were achieved by applying negative and positive external voltage.

The current-voltage (I-V) characteristics of as prepared AZO/BT-BNN/Ag device were measured by using electrometer in dark and under light illumination. Since, the band gap (E_{g1}) of 0.70BT-0.30BNN is 2.26 eV, the photons having wavelength less than 548 nm can only stimulate the electron-hole pairs. The second threshold band gap (E_{g2} =1.3 eV) can facilitate the possibility to absorb the photons having wavelength less than 953 nm. For light illumination, green laser (λ = 532 nm) light and visible light with light intensity 100 mW/cm^2 were used to investigate the photovoltaic properties of BT-BNN ceramics.

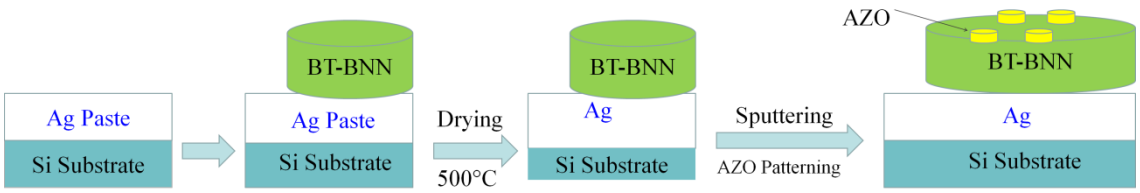

FIGURE 5.11 A Schematic illustration of various fabrication process steps of AZO/BT-BNN/Ag heterojunction device on silicon substrate.

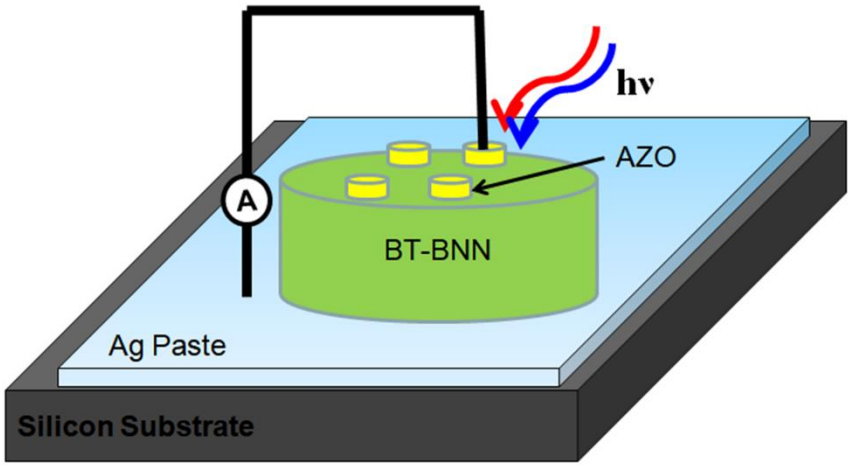

FIGURE 5.12 A schematic representation of the AZO/BT-BNN/Ag heterojunction device.

Fig. 5.13 shows the I-V curves of AZO/0.70BT-0.30BNN/Ag device in dark and under different light illumination intensity. The sample was positively poled and I-V measured with varying the light illumination intensity (I_1 = 50 mW/cm^2, I_2 = 70 mW/cm^2, I_3 = 100 mW/cm^2). Fig. 5.13 illustrates a systematic increment in short circuit current density (J_{sc}). Under dark, device shows very low current without open circuit voltage (V_{oc}). Under light illumination device shows the photovoltaic behaviour. At 50 mW/cm^2 light illumination intensity, J-V curve of device shows a short –circuit current density (J_{sc}) of 0.087 µA/cm^2 and open-circuit voltage (V_{oc}) of -1.45 V. The PV

mechanism in dark and under light illumination is explained using schematic diagram of AZO/BT-BNN/Ag heterostructure as illustrated in Fig.5.14. In dark condition (absence of light), due to thermionic emission few randomly generated electrons move from bottom electrode towards top and generate the small amount of current which flows into the device as shown in Fig 5.14 (a).

When light is illuminated on AZO top side, the BT-BNN surface becomes conductive and photo-induced charge carriers are generated. The internal electric field in BT-BNN layer separates the photo-generated electronic charge carriers. Then, the electrons from the BT-BNN layer are transferred to the Ag electrode and holes are transferred to AZO electrode as illustrated in Fig.5.14 (b). The transportation of electrons and holes gives rise to a photocurrent at zero external bias voltage. Fig 5.13 shows the incident light illumination intensity dependent J-V curve along with the dark current. It shows the increase in short-circuit current density (J_{sc}) with increasing the light intensity from 50 mW/cm^2 to 100 mW/cm^2. Light intensity plays important role in producing the photo-carriers in semiconducting layer, Increasing the illumination light intensity can produce more photo-carriers (electron-hole pairs), which are then separated by the internal field and lead to larger J_{sc}.

According to theoretical model, the photocurrent is proportional to intensity of light I, which follows the relation; current density $J = k\alpha I$, where ‘α’ is the light absorption coefficient and ‘k’ is the glass constant which depends on the nature of the absorbing local environment [A. M. Glass et al. (1975)]. At low light intensity (50 mW/cm^2), J_{sc} is 0.087 μA/cm^2 which increased 5.6 times (J_{sc} =0.49 μA/cm^2) for 70 mW/cm^2 light intensity. Under weak light illumination, less number of photons reach at BT-BNN surface and result in low generation of photo-carriers.

The effect of light intensity on photovoltaic mechanism is illustrated in Fig. 5.15 using the schematic energy band diagram. Fig 5.15 (a) explain the photovoltaic mechanism during low intensity light illumination where less number of electrons and holes are generated and field due to polarization plays dominant role. Fig 5.15 (a) and (c) show the photo-voltaic mechanism, when, the light intensity is increased. From Fig. 5.15, it is clear that increasing light intensity can generate more electron-hole pairs, which are separated by internal field and lead to larger I_{sc}. At 100 mW/cm^2 light illumination intensity, J-V curve of device shows a short –circuit current density (J_{sc}) of 1.5 μA/cm^2 and open-circuit voltage (V_{oc}) of -1.49 V. There is nearly 17 times increment in J_{sc} value of device when light intensity is increased from 50 mW/cm^2 to 100 mW/cm^2. The light intensity dependent photovoltaic behaviour also provides the evidence of bulk-photovoltaic effect in BT-BNN ferroelectric device. We have observed that photo-current linearly increased with increasing the light intensity but open circuit voltage (V_{oc}) is not much affected. Only slight increase (0.04V) is obtained with increasing the light intensity from 50 mW/cm^2 to 100 mW/cm^2.

The open circuit voltage (V_{oc}) is related to following equation [D. Pang et al. (2018)]

$$V_{oc} = \frac{G\alpha I}{\sigma_d + \sigma_{ph}} d$$

Where 'I' is light intensity, σ_d is dark conductivity σ_{ph} is photo conductivity of the ferroelectric material, 'G' is glass coefficient and 'α' is absorption coefficient, d is thickness. At low light intensity, the σ_{ph} is considered almost constant, so V_{oc} increase with light intensity but later saturated. In BT-BNN based heterostructure, the V_{oc} can be considered almost constant with increasing the incident light intensity and thus it can be concluded that it is a signature of bulk photo-voltaic effect (BPVE) [J. E. Spanier et al. (2016); Z. Gu et al. (2017); S. Pal et al. (2018)].

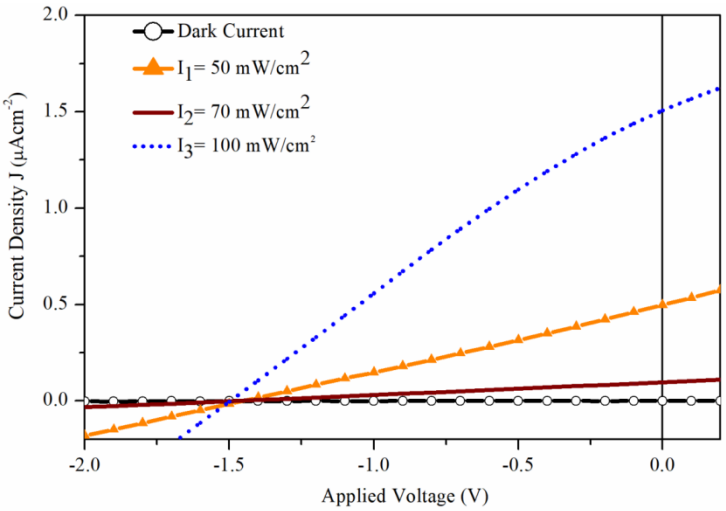

Figure 5.13 J-V curves of AZO/BT-BNN/Ag devices in dark and under different light intensity after positive poling.

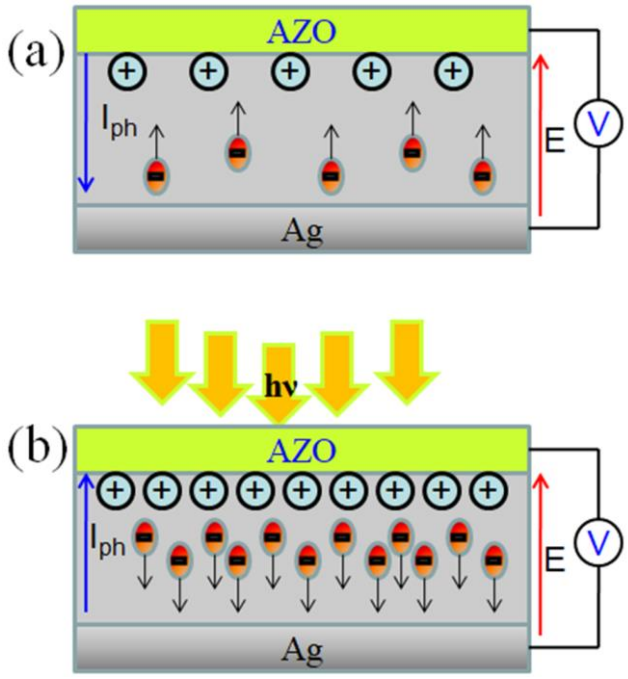

Figure 5.14 Photovoltaic mechanisms in AZO/BT-BNN/Ag heterojunction device in (a) dark and (b) under light conditions**.** The photocurrent is mentioned as I_{ph} and E is electric field.

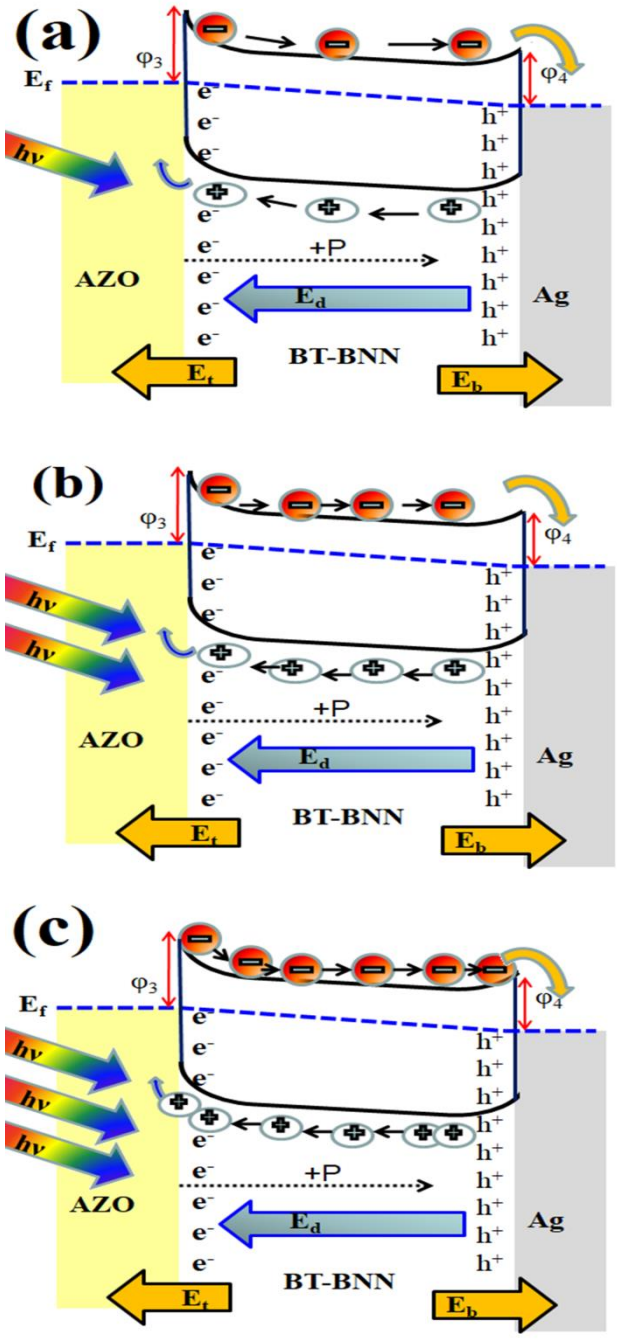

Figure 5.15 Schematics of energy band diagram and photovoltaic mechanism of AZO/BT-BNN/Ag/Si device under various light illumination intensity (a) 50mW/cm^2 (b) 70mW/cm^2 and (c) 100mW/cm^2. E_f, E_{cb} and E_{vb} represent Fermi energy level, conduction band and valence band respectively. Dotted arrow represents the applied polarization direction and big blue arrow shows the depolarization field direction.

5.3.6 Switchable Photovoltaic Behaviour of AZO/BT-BNN/Ag Device

The switchable photovoltaic behaviour is signature of BPVE in materials. It is well known that various factors, such as, interface Schottky barriers, polarization, domain structures, and domain walls affect the photovoltaic parameters of ferroelectric devices [W. Ji et al. (2010); L. Fang et al. (2014); A. Bhatnagar et al. (2013)]. In order to measure the effect of depolarization field, I-V is measured for unpoled, positively poled and negatively poled samples. As shown in Fig. 5.16, J-V curve of $0.60BaTiO_3$-$0.40Bi(Ni_{2/3}Nb_{1/3})O_3$ ceramic device with unpoled, positively and negatively poled samples showing switchable photovoltaic effect. In unpoled condition, device shows J_{sc} = 0.04 μA/cm^2 and V_{oc} = -0.27V which increased to J_{sc} = 1.068 μA/cm^2 and V_{oc} = -1.38V after positive poling. The negatively poled sample shows J_{sc} = -0.18 μA/cm^2 and V_{oc} = +0.74V. The observed switchable I_{sc} and V_{oc} confirm the effect and role of depolarization field on photovoltaic phenomenon. The difference in V_{oc} values for positively and negatively poled samples is due to contribution of Schottky barrier height in PV mechanism. Similar behaviour is also reported for Au/$BiFeO_3$/ITO heterostructure [Y. Zhou et al. (2020)].

The low V_{oc} in unpoled AZO/BT-BNN/Ag device can be attributed to randomly oriented dipoles, and its mechanism is explained by possible model using the energy band diagram as shown in Fig 5.17 (a). In unpoled devices, the net built-in field depends on top and bottom Schottky barrier difference. Two back-to-back Schottky barriers are built at the BT-BNN/electrode interface due to difference between the work function of ferroelectric pellet and electrodes [J. Zhang et al. (2013); K. Wang et al. (2016)]. As both top and bottom electrodes are different and have different work function, the Schottky barriers will be different and it will form asymmetrical Schottky barriers [Z. Tan et al. (2019)]

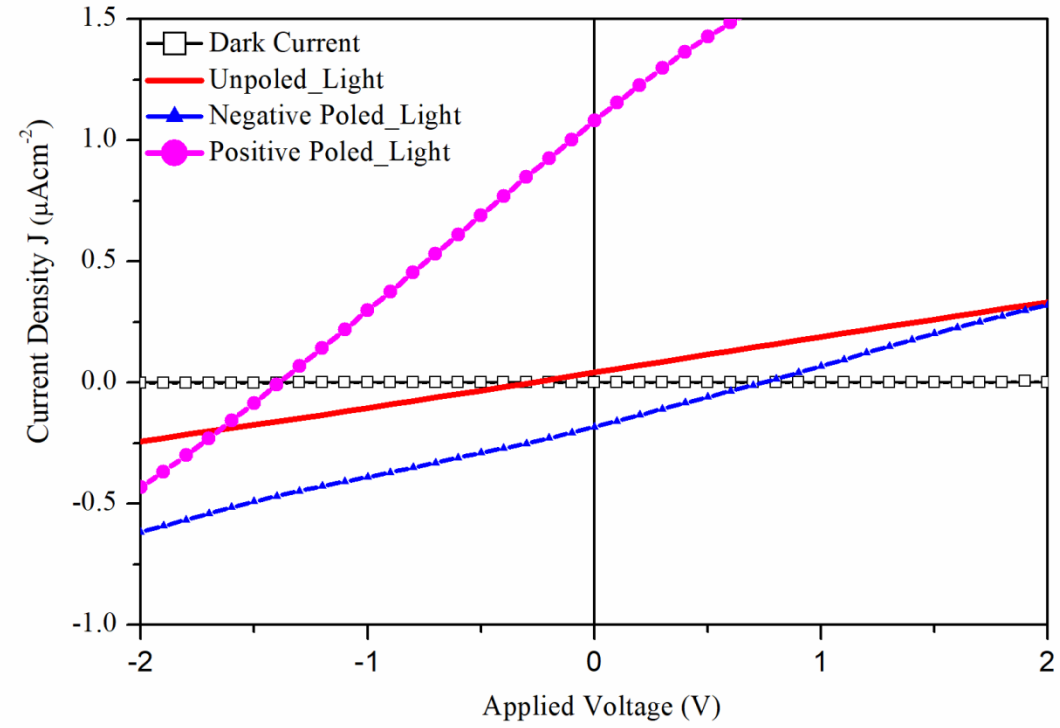

FIGURE 5.16 J-V curve of $0.60BaTiO_3$-$0.40Bi(Ni_{2/3}Nb_{1/3})O_3$ ceramic device with unpoled, positively and negatively poled samples showing switchable photovoltaic effect. Black open squares are for the J-V curve in dark, red line indicates the J-V curve of device before poling, blue filled triangles and magenta filled circles indicate J-V curves of devices with negative and positive poling.

In present work, AZO/BT-BNN/Ag devices have two interfaces: AZO/BT-BNN and BT-BNN/Ag, they have Schottky electrical field at the interfaces termed as E_t and E_b respectively. Based on previous reports, the work function (φ_{AZO}) of AZO is 4.62 eV and work function (φ_{Ag}) of Ag is 4.26 eV that is considered to construct the band diagram [A. B. Swain et al. (2019)]. The top and bottom interfacial Schottky barriers are calculated using the electron affinity (χ) of BT-BNN. The top interface has interfacial Schottky barrier ($\varphi_1 = \varphi_{AZO} - \chi_{BT} = 0.72$). The bottom interface has interfacial Schottky barrier ($\varphi_2 = \varphi_{Ag} - \chi_{BT} = 0.36$). The difference between these two Schottky

barrier heights at top and bottom interfaces give the internal net potential ($\Delta\varphi_{AZO/BT/Ag}$ = φ_{AZO} - φ_{Ag} = 0.36 eV) which is the built-in field in the device due to the presence of different electrode materials. The Schottky barrier difference for polycrystalline ferroelectric materials is reported to be usually lower than the theoretical values [M. Qin et al. (2009)]. As samples are unpoled so depolarization field is not active. The obtained low V_{oc} (-0.27 V) is reasonable for unpoled device. Taking into account the Schottky barriers at the top and bottom interface, the energy band diagram of AZO/BT-BNN/Ag heterostructure is illustrated in Fig. 5.17(a). The Schottky barrier space charge field E_t and E_b pointing at interfaces help to separate and transport the photo-carriers to their respective electrode.

Fig. 5.17 (b) illustrates the energy band diagram of AZO/BT-BNN/Ag after positive poling. Built-in-field which formed at AZO/BT-BNN and BT-BNN/Ag interfaces are termed as E_t and E_b, respectively. Depolarization field (E_d) is opposite to applied polarization P. E_f, E_{cb} and E_{vb} are Fermi energy level, conduction band and valence band, respectively. The net internal electric fields in AZO/BT-BNN and BT-BNN/Ag interfaces will be E_t+E_d and E_b-E_d, respectively, after positive poling. Therefore, the barrier height of AZO/BT-BNN interface will be increased. The barrier height of BT-BNN/Ag interface will reduce for positively polarized samples. So, the barrier height φ_3 is higher than φ_4 ($\varphi_3 > \varphi_4$) as drawn schematically in Fig. 5.17 (b). The barrier height φ_4 is decreased after positive poling of the sample because the positive charges will be accumulated near BT-BNN/Ag interface and can shift the energy levels of BT-BNN down. Thus, increased surface charges can reduce φ_4 and can increase the φ_3. The photo-induced electrons will flow towards Ag electrode and holes will flow towards AZO electrode, resulting in photo-current. As barrier height φ_4 is lower, so it will provide smooth transportation of electrons flow and thus external circuit will give

higher current. As the direction of net Schottky electric field and depolarization field are same the net internal built-in potential will be much higher and give higher open circuit voltage.

The net internal electric fields in AZO/BT-BNN and BT-BNN/Ag interfaces will be E_t-E_d and E_b+E_d respectively after negative poling as the direction of depolarization field will be reversed. Therefore, the barrier height of BT-BNN/Ag interface will be increased. The barrier height of AZO/BT-BNN interface will reduced for negatively polarized samples. So, the barrier height φ_6 will be higher than φ_5 ($\varphi_6 > \varphi_5$) as schematically drawn in Fig. 5.17 (c). Even though the barrier height is lower but due to low internal electric field the charge separation process will be slowed down and a smaller number of electrons and holes will transport towards their respective electrodes.

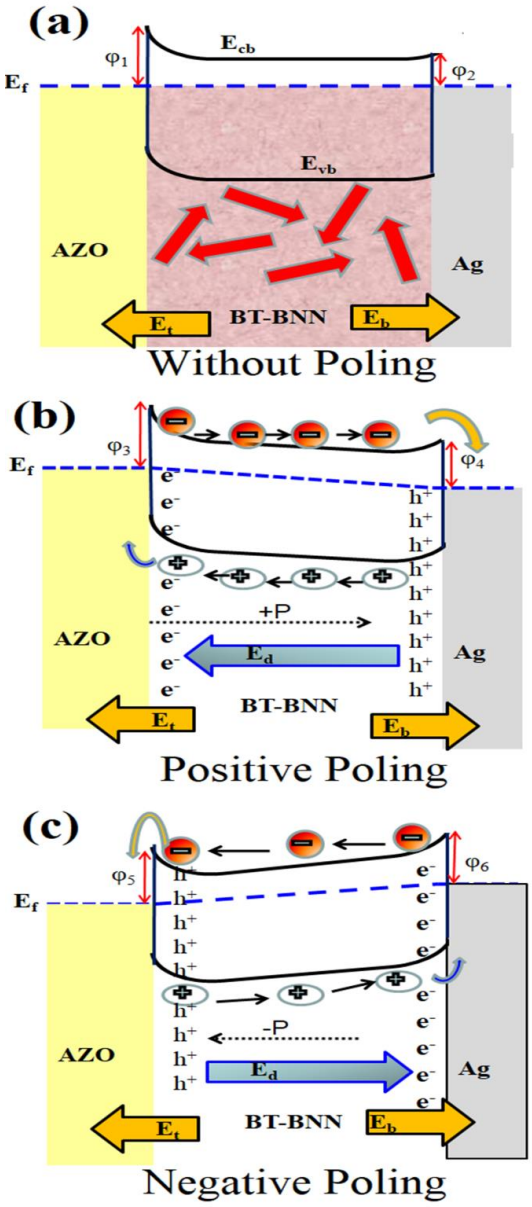

Figure 5.17 Schematic of energy band diagram with internal electric field distribution and mechanism of the photovoltaic effect of AZO/BT-BNN/Ag device with interfacial layers in (a) Unpoled state (b) positively poled state and (c) negatively poled state. Built-in-field formed at AZO/BT-BNN and BT-BNN/Ag interface is termed as E_t and E_b. Depolarization field is termed as E_d which is opposite to applied polarization P. E_f, E_{cb} and E_{vb} are Fermi energy level, conduction band and valence band respectively. Large red coloured arrows represent the random direction of polarization in unpoled state.

5.3.7 Compositional Dependent J-V Characteristics of AZO/BT-BNN/Ag Heterostructure

In order to study the compositional dependence of photovoltaic properties of xBT-(1-x)BNN solid solutions, AZO/BT-BNN/Ag devices were fabricated for various compositions (x = 0.92, 0.85, 0.80, 0.75, 0.70, and 0.60) and current-voltage characteristics were measured after positive poling of devices. The current density–voltage (J-V) characteristics of the BT-BNN hetero-structures under light illumination are shown in Fig.5.18. After light illumination the BT-BNN surface becomes conductive and photo-induced charge carriers are generated. The photo-carriers are separated and accelerated by build-in-field (interface field and depolarization field). As observed from Fig, 5.18, the open circuit voltage depends on polarization of BT-BNN compositions. The produced photo-current depends on remnant polarization and band gap of BT-BNN ceramic. Even though the 0.92BT-0.08BNN and 0.80BT-0.20BNN have higher remnant polarization and high photo-induced electric field, but, both devices shows low photocurrent which is due to their low absorption ability of light and high band gap.

The composition 0.92BT-0.08BNN have J_{sc} = 0.126 μA/cm^2 and V_{oc} = -3.23V, 0.85BT-0.15BNN have J_{sc} = 0.294 μA/cm^2 and V_{oc} = -2.63V and 0.80BT-0.20BNN shows J_{sc} = -0.433 μA/cm^2 and V_{oc} = -1.97 V. In polycrystalline materials, even though the direct band gap is more than 3.0 eV still it shows the photocurrent. The generation of photo-induced charge carriers in 0.92BT-0.08BNN is due to presence of vacancies at grain boundaries whose ionization energy is usually smaller than band gap of material [(2015)]. As BNN doping percentage increases the V_{oc} value is also decreased due lowering of polarization in BT-BNN. The highest photocurrent (J_{sc} = 1.5 μA/cm^2) is

observed for 0.70BT-0.30BNN composition. However, 0.70BT-0.30BNN composition has lower V_{oc} (-1.49V) as compare to 0.92BT-0.08BNN.

The J-V curve shows deviation from linear behaviour which gives the evidence of Schottky contacts between AZO and BT-BNN surface. Another composition 0.60BT-0.40BNN has the lowest band gap (= 2.19 eV) but it shows the lowest V_{oc} (-1.38 V) and photocurrent J_{sc} (1.068 μA/cm^2) is also reduced as compared to the other composition (x=0.70). The decrease in J_{sc} for 0.60BT-0.40BNN can be related to its poor spontaneous polarization. Due to low polarization, the process of charge separation and transportation slows down and decrease in photo-current is expected. Due to low depolarization field, the charge recombination may also occur. Thus, the V_{oc} is highly dependent on polarization magnitude of the material and it reduces from -3.23 V to -1.38 V with increasing BNN doping concentration. As discussed in section 5.3.3, the remnant polarization of BT-BNN reduces with increasing the BNN doping concentration. The depolarization field E_d is proportional to the polarization strength of corresponding material and is given by following equation

$$E_d = -\frac{P}{\varepsilon_0 \varepsilon_F}\left(\frac{\varepsilon_F/d}{2\varepsilon_F/d + \varepsilon_e/\lambda}\right)$$

Where P is value of polarization, d is ferroelectric film layer thickness, ε_F is the relative dielectric constant of the ferroelectric layer, ε_e is dielectric constant of the electrode layer, and λ is the screening length of the electrode [D. J. Kim et al. (2005)]. From experimental results, it can be concluded that V_{oc} directly depends on remnant polarization of material and J_{sc} is related to both the band gap and polarization. The photo-induced electric field (E_{pv}) for 0.92BT-0.08BNN is calculated to be around 53.8 V/cm which reduces with increasing the BNN doping concentration. The 0.60BT-

0.40BNN shows low photoinduced electric field value ~23V/cm while the highest photo-current (J_{sc}~1.5 μA/cm^2) is obtained for 0.70BT-0.30BNN which has higher polarization. The band gap values of both these compositions are very close, 0.60BT-0.40BNN have band gaps (E_{g1} ~2.19 eV, E_{g2} ~ 1.32 eV) while 0.70BT-0.30BNN have slightly higher direct band gap (E_{g1} ~2.26 eV, E_{g2} ~ 1.28 eV). Here, secondary band gap of BT-BNN plays important role which has lower value for 0.70BT-0.30BNN as compared to 0.60BT-0.40BNN composition. During light illumination, the photo-carriers are easily created, separated and transported in low band gap materials. The low band gap materials usually have smaller excitons bonding energy and thus results in higher generation of photocurrent [L. Azzouz et al. (2019)]. Thus, even though the low band gap BT-BNN composition (x =0.70, and 0.60) have lower polarization strength still they show higher current as compare to compositions (x =0.92, and 0.85) which have high polarization strength but wide band gap.

The obtained E_{pv} for BT-BNN is much less than the corresponding coercive field and intrinsic Landau-Ginzburg value (10^6 V/cm) for $BaTiO_3$ [V. Fridkin (2014)]. The higher thickness of our polycrystalline BT-BNN samples in device is the primary reason for low photocurrent and low light to current device efficiency. The device efficiency can be increased by either using very thin pellet or thin films of BT-BNN.

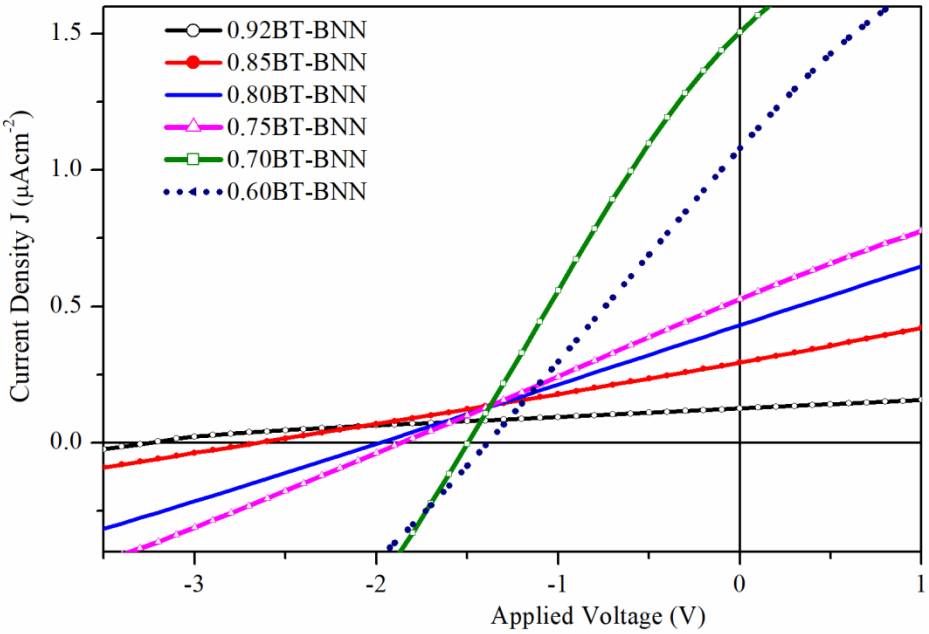

Fig.5.18 Composition dependent J-V curves of AZO/BT-BNN/Ag devices after positive poling. J-V characteristic curves of heterostructure with BT-BNN layer having different band gap demonstrating the photovoltaic effect.

5.4 Conclusions

In this work, $xBaTiO_3$-$(1-x)Bi(Ni_{2/3}Nb_{1/3})O_3$ solid solution in the composition range ($0.50 \leq x \leq 0.92$) were successfully prepared by solid state ceramic synthesis and characterized for crystal structure, optical and ferroelectric properties. The unit cell parameter and bond lengths exhibit significant change with changing the composition. The band gap is significantly reduced from 3.2 eV to 2.19 eV for BNN doped $BaTiO_3$. This work provides good insights for the band gap tuning of $BaTiO_3$ with varying the concentration of $Bi(Ni_{2/3}Nb_{1/3})O_3$. The local ferroelectric switching is observed in BT-BNN ceramics which is reduced with BNN doping. The current-voltage (I-V) characteristics of as prepared AZO/BT-BNN/Ag device were measured in dark and under light. We have demonstrated polarization direction dependent photovoltaic behaviour and bulk photo-voltage in BT-BNN based device. Our discovery of switchable ferroelectric diode effect in lead free polycrystalline ceramic BT-BNN may

provide an opportunity for designing new electronic devices. The observed polarization and band gap dependent photo-current, switchable photovoltaic effect of BT-BNN will be of great interest for future ferroelectric photovoltaic devices.

.